Materials Today Nano 35 (2026) 100945

Contents lists available at ScienceDirect

Materials Today Nano

journal homepage: www.sciencedirect.com/journal/materials-today-nano

Laser-induced graphene electrodes/Nd-MOF hybrid platform for selective electrochemical detection of cancer cells

Melek Salmanli [a,b], Bilge Ölçeroglu [a,b], Deniz Sakarya [a,b], Eray Tabak [a,b], Furkan Albora [a,b], Yasemin Kaptan [c], Demet Sezgin Mansuroglu [d], Dursun Yasar Bayramli [e], Serdar Sanli [f,*], Sahika Sena Bayazit [a,b,**], Firat Baris Barlas [a,b,g,***]

[a] Institute of Nanotechnology and Biotechnology, Istanbul Univeristy-Cerrahpasa, Istanbul, 34500, Türkiye
[b] Health Biotechnology Joint Research and Applications Center of Excellence, Istanbul, 34220, Türkiye
[c] Department of Chemical Engineering, Faculty of Engineering & Architecture, Istanbul Beykent University, Istanbul, 34398, Türkiye
[d] Department of Chemistry and Chemical Processing Technologies, Kocaeli Vocational School, Kocaeli University, 41140, Türkiye
[e] Espiye Vocational School, Giresun University, Giresun, 28200, Türkiye
[f] Department of Chemistry, Faculty of Arts and Sciences, Ordu University, Ordu, 52200, Türkiye
[g] Clinical Research Excellence Application and Research Center, Istanbul Univeristy-Cerrahpasa, Istanbul, 34098, Türkiye

ARTICLE INFO

Keywords:
Laser-induced graphene
Neodymium-based MOF
Folic acid functionalization
Electrochemical biosensor

ABSTRACT

In this study, a novel electrochemical biosensing platform was developed for the selective detection of cancer cells based on a laser-induced graphene (LIG) electrode modified with neodymium-based metal–organic frameworks (Nd-MOFs). The Nd-MOF structures were synthesized using aminoterephthalic acid and subsequently functionalized with folic acid (FA) via EDC/NHS coupling to enable targeted recognition of folate receptor-overexpressing cells. The hybrid Gr/Nd-MOF-FA interface combines the conductive graphene framework with the high surface area and abundant functional sites of the Nd-MOF, enabling efficient folic acid immobilization and selective cancer cell recognition. The physicochemical properties of the synthesized materials were characterized using FTIR, XRD, and SEM analyses, confirming successful MOF formation, amine functionalization, and FA conjugation. Electrochemical behavior was systematically evaluated using cyclic voltammetry (CV), differential pulse voltammetry (DPV), and electrochemical impedance spectroscopy (EIS). The developed biosensor exhibited a strong and selective response toward folate receptor-overexpressing HeLa cells, while only negligible interaction was observed with the folate receptor-low A549 cell line, confirming the selective recognition enabled by folic acid functionalization. The sensor demonstrated a sensitive detection capability with a limit of detection (LOD) of 236 cells for the HeLa cell line. Fluorescence imaging and proliferation assays further supported the biocompatibility and targeted interaction of the functionalized surfaces. Additionally, LIG surfaces exhibited intrinsic fluorescence properties attributed to graphene composite, enabling potential integration of optical sensing capabilities. Overall, this study presents a multifunctional and highly sensitive biosensing platform that combines electrochemical and optical features. The proposed platform may serve as a versatile tool for evaluating for future investigations into cancer cell detection, cell monitoring, and other biomedical applications, including diagnostic and theranostic strategies.

1. Introduction

Metal–organic frameworks (MOFs) are a class of crystalline porous materials formed through the coordination of metal ions or metal clusters with multidentate organic linkers, resulting in highly ordered three-dimensional architectures. Owing to their exceptionally high surface areas—often exceeding 6000 m^2 g^{-1}—along with tunable pore size distribution and chemical functionality, MOFs have emerged as versatile platforms across a wide range of applications, including gas storage and separation, catalysis, sensing, and biomedical imaging [1]. The

* Corresponding author.
** Corresponding author. Institute of Nanotechnology and Biotechnology, Istanbul Univeristy-Cerrahpasa, 34500, Istanbul, Türkiye.
*** Corresponding author. Institute of Nanotechnology and Biotechnology, Istanbul Univeristy-Cerrahpasa, 34500, Istanbul, Türkiye.
E-mail addresses: serdarcansanli@gmail.com (S. Sanli), sahika.bayazit@iuc.edu.tr (S.S. Bayazit), fbbarlas@iuc.edu.tr (F.B. Barlas).

https://doi.org/10.1016/j.mtnano.2026.100945
Received 4 May 2026; Received in revised form 9 August 2026; Accepted 1 September 2026
Available online 1 September 2026
2588-8420/© 2026 Published by Elsevier Ltd.

structural modularity of MOFs allows precise control over their physicochemical properties, rendering them particularly attractive for analytical and bioanalytical applications where selectivity and sensitivity are critical.

Beyond conventional transition metal-based MOFs, lanthanide-based MOFs (Ln-MOFs) have garnered increasing attention due to their unique electronic configurations and outstanding photophysical properties [2]. Among these, neodymium-based MOFs (Nd-MOFs) represent a particularly promising subclass. The Nd^{3+} ion, characterized by its $4f^3$ electronic configuration, exhibits distinctive near-infrared (NIR) luminescence properties, which are highly advantageous for biological applications due to minimal background interference and deeper tissue penetration [3]. Furthermore, the high and flexible coordination number of Nd^{3+} ions (typically ranging from 8 to 12) facilitates the formation of structurally complex and robust frameworks, particularly when integrated onto electrode surfaces. Importantly, the 4f orbitals of lanthanides are effectively shielded by outer electron shells, which minimizes environmental perturbations and contributes to the chemical stability and reproducibility of Nd-MOF-based systems under physiological conditions [4,5].

In the context of electrochemical biosensing, the intrinsic limitations of MOFs—such as relatively low electrical conductivity—can be effectively addressed through hybridization with highly conductive carbon-based nanomaterials, particularly graphene [6]. Graphene, a two-dimensional (2D) material with exceptional electrical conductivity, mechanical strength, and large specific surface area, serves as an ideal scaffold to enhance electron transfer kinetics. The integration of MOFs with graphene provides complementary functional advantages by combining the high porosity and chemical versatility of MOFs with the excellent electrical conductivity of graphene. Moreover, self-assembled 2D MOF layers on graphene-modified electrode surfaces provide a well-defined and biocompatible interface for biomolecule immobilization [7].

Laser-induced graphene (LIG) has emerged as a versatile and scalable approach for the direct fabrication of porous, conductive graphene structures on polymeric substrates, particularly polyimide, via localized photothermal conversion using CO_2 laser irradiation. This mask-free and single-step process enables simultaneous carbonization and graphitization, resulting in three-dimensional, interconnected graphene networks with high surface area, tunable porosity, and excellent electrical conductivity [8,9]. The structural and physicochemical properties of LIG can be precisely controlled by adjusting laser parameters such as power, scan speed, and pulse density, allowing the formation of functional micro- and nanoscale patterns tailored for specific applications [10]. Beyond its simplicity and cost-effectiveness, LIG offers significant advantages in terms of rapid prototyping and compatibility with flexible and wearable platforms. Recent studies have demonstrated its broad applicability in electrochemical sensing, energy storage, microfluidic systems, and biomedical interfaces, owing to its unique combination of conductivity, mechanical robustness, and surface functionalization capability [11]. These attributes position LIG as a promising material platform for next-generation electronic, optoelectronic, and biosensing devices.

Targeted detection of cancer cells using electrochemical biosensors requires the incorporation of selective recognition elements. In this regard, folic acid (FA) has been widely employed as a targeting ligand due to its high affinity for folate receptors (FRs), which are overexpressed in various cancer cell types, including cervical cancer-derived HeLa cells [12,13]. The covalent conjugation of FA onto nanostructured platforms is commonly achieved via carbodiimide chemistry (EDC/NHS), enabling stable amide bond formation between FA and functional groups present on the nanomaterial surface. This functionalization strategy significantly enhances the selectivity of the biosensor by enabling receptor-mediated recognition.

In the present study, self-assembled Nd-MOF structures were synthesized and immobilized onto graphene-modified electrode surfaces to construct a hybrid electrochemical sensing platform. The resulting Nd-MOF/graphene interface was subsequently functionalized with folic acid to enable targeted recognition of folate receptor-positive cancer cells. The analytical performance of the developed biosensor was systematically evaluated using folate receptor-overexpressing HeLa cells as the target model and A549 cells as a negative control due to their relatively low folate receptor expression. The integration of Nd-MOFs with graphene provides a dual advantage: enhanced electrochemical signal amplification arising from the high surface area and redox-active nature of the MOF structure, and accelerated electron transfer enabled by the conductive graphene network. Combined with FA-mediated targeting, this system offers a highly biocompatible, sensitive and selective platform for cancer cell detection. Overall, this work highlights the potential of lanthanide-based MOF hybrids as next-generation electrochemical biosensing systems with significant implications for early cancer diagnostics and precision medicine.

2. Material and methods

All chemicals were of analytical grade and used without further purification. Neodymium(III) nitrate hexahydrate ($Nd(NO_3)_3{\cdot}6H_2O$), terephthalic acid, nitroterephthalic acid, tin(II) chloride ($SnCl_2$), acetic acid, sodium dodecyl sulfate (SDS), 3-(4,5-dimethylthiazol-2-yl)-2,5-diphenyltetrazolium bromide (MTT), and phosphate-buffered saline (PBS) components (NaCl, KCl, Na_2HPO_4, KH_2PO_4) were purchased from Sigma-Aldrich (MERCK), N,N-Dimethylformamide (DMF) was obtained from Isolab, Distilled water was obtained using a Millipore purification system.

2.1. Synthesis of 2-aminoterephthalic acid

A three-neck round-bottom flask was loaded with TP (20 g) and concentrated sulfuric acid (60 mL, 95–98%). While maintaining the mixture at 0 °C under continuous stirring, nitric acid (15 mL, 65%) was slowly introduced over a period of 1 h. The reaction temperature was then gradually raised to 60 °C and held for 1 h. Afterward, the temperature was further increased to above 80 °C within 1 h and maintained at this level overnight. Upon completion, the reaction mixture was quenched by the addition of ice water. The resulting solid was collected by filtration and thoroughly washed with 3 L of distilled water. The crude material was purified by recrystallization from 1 L of acetone, in which NTP is soluble whereas TP remains insoluble. The purified solid was isolated by filtration and dried at 60 °C to afford 2-nitroterephthalic acid (NTP). For the reduction step, a three-neck round-bottom flask was charged with fuming hydrochloric acid (80 mL, 37%), followed by the gradual addition of tin(II) chloride dihydrate (30 g) under stirring. Subsequently, NTP (10 g) was added to the mixture, and the reaction was carried out at 80 °C for 6 h. After the reaction, the mixture was filtered, and the solid residue was washed with distilled water. The product was then dried in an oven at 60 °C for 2 h to obtain ATP. The final product was obtained as a lemon-yellow powder with a yield of 9.83 g (45%) and a melting point above 300 °C [14].

2.2. Synthesis of Nd-MOF

Nd-MOFs were synthesized using neodymium nitrate hexahydrate ($Nd(NO_3)_3{\cdot}6H_2O$) and 2-aminoterephthalic acid as precursors. Both components were dissolved in 50 mL of N,N-dimethylformamide (DMF) and subjected to ultrasonication to obtain a homogeneous solution.

The resulting mixture was transferred into a stainless steel-lined autoclave and incubated at 120 °C for 24 h under solvothermal conditions. After naturally cooling to room temperature, the obtained solid product was collected by filtration using a Gooch crucible. The precipitate was thoroughly washed with ethanol to remove residual DMF and unreacted species, followed by air-drying at room temperature for 2 h. The drying process was then continued under vacuum at 80 °C for 12 h

to obtain the final Nd-MOF material.

2.3. Folic acid functionalization via EDC/NHS coupling

Folic acid (FA) is widely used as a targeting ligand in biosensing and drug delivery systems due to its high affinity toward folate receptors, which are overexpressed in various cancer cells. In this study, the surface of the synthesized Nd-MOF structures was functionalized with FA to enhance selective binding toward target cells. Covalent conjugation of FA onto Nd-MOFs was achieved using carbodiimide chemistry (EDC/NHS coupling). Briefly, 0.05 M EDC and 0.125 M NHS solutions were prepared in citrate buffer. Subsequently, 30 mg of folic acid and 50 mg of Nd-MOF were added to the reaction mixture and stirred for 1 h to allow activation and initial interaction. Following this step, the EDC and NHS-activated system was allowed to react for a total of 3 h under continuous stirring to facilitate amide bond formation between the activated carboxyl groups of FA and the free amine groups present on the MOF surface.

2.4. Conjugation efficiency

The conjugation efficiency of folic acid (FA) onto Nd-MOF structures was determined using UV–Vis spectrophotometry. FA exhibits a characteristic absorption peak in the UV region (280–285 nm), and all measurements were performed at 280 nm [15] A calibration curve was established using known concentrations of FA to obtain a linear relationship between absorbance and concentration. Following EDC/NHS-mediated conjugation, the reaction mixture was transferred into a dialysis membrane and dialyzed against PBS overnight at 4 °C to remove unbound FA molecules.

After dialysis, the amount of unbound FA that diffused through the membrane was quantified by measuring the absorbance of the external solution at 280 nm. The decrease in FA concentration relative to the initial amount was attributed to FA successfully conjugated onto the Nd-MOF surface.

The conjugation efficiency (CE%) was calculated using the following equation:

$$CE\ (\%) = ((C_0 - C_s)\ /\ C_0) \times 100$$

where C_0 represents the initial concentration of FA before conjugation and C_s corresponds to the concentration of free (unbound) FA detected after dialysis.

2.5. Manufacturing of laser-induced graphene (LIG) electrode

Laser-induced graphene electrodes were fabricated using a approach based on the direct laser scribing of polyimide substrates. Commercial polyimide (Kapton®) films (thickness ~125 μm, DuPont) were used as the carbon precursor. All chemicals employed in this study were of analytical grade and used without further purification. Deionized water (18.2 MΩ cm) was utilized in all experimental procedures. For electrochemical characterization, potassium ferricyanide/potassium ferrocyanide ($[Fe(CN)_6]^{3-}/^{4-}$) redox probe and potassium chloride (KCl) were used to prepare the electrolyte solution.

LIG structures were generated by irradiating the surface of the polyimide film using a Diode laser engraving system operating at a wavelength of 450 nm. The laser parameters, including power, scan speed, and resolution (Longer Ray5 diode laser system; LightBurn Core 2.0.05 software; printing speed 15,000 mm/min; 5 W laser at 30% power; 0.05 mm scan interval; laser distance 3 cm; for low-density regions, 10% power is sufficient). During the laser irradiation process, localized photothermal heating led to rapid carbonization and graphitization of the polyimide substrate, resulting in the formation of a porous, three-dimensional graphene network. The electrode geometry was defined through computer-aided design, allowing precise patterning of the working area directly onto the substrate without the need for additional lithographic steps.

Following laser processing, the electrodes were gently rinsed with deionized water to remove residual debris and dried under a nitrogen stream. Electrical contacts were established using conductive silver paste, and the non-active regions of the electrode were insulated with an inert polymer coating to ensure well-defined electrochemical measurements.

For biological applications, the electrodes were sterilized under ultraviolet irradiation prior to use. In selected experiments, surface functionalization strategies were employed to enhance cell adhesion and targeting efficiency. Human cancer cell lines, including A549 and HeLa, were cultured on the electrode surfaces under standard incubation conditions (37 °C, 5% CO_2). Cell attachment and proliferation were subsequently evaluated through fluorescence imaging and electrochemical signal variations.

All experiments were performed in triplicate, and the obtained data were expressed as mean ± standard deviation. Statistical analyses were conducted to evaluate the reproducibility and significance of the results, with a p-value below 0.05 considered statistically significant.

2.6. Characterization

UV–Vis absorption spectra were recorded using a Jasco V-730 spectrophotometer at 276 nm to investigate the optical properties and potential drug loading/release characteristics.

Differential scanning calorimetry (DSC) measurements were carried out using a PerkinElmer DSC 6002 instrument over a temperature range of −30 to 300 °C at a heating rate of 10 °C min^{-1} to analyze thermal transitions.

Powder X-ray diffraction (XRD) patterns were obtained using a Rigaku SmartLab X-ray diffractometer to assess the crystallinity and phase structure of both pristine Nd-NH_2-MOF and functionalized MOF samples.

2.6.1. SEM imaging and elemental mapping

Scanning electron microscope (SEM) analyses were carried out using a Thermo Fisher Quattro S to assess the size of the Nd-MOF, Nd-MOF-FA, Gr, Gr/Nd-MOF and Gr/Nd-MOF-FA. Also, elemental mapping carried out a Brucker EDS.

2.6.2. Raman spectroscopy

Raman spectroscopy was performed using a Thermo Fisher Raman spectrometer to confirm the formation and graphitization of the laser-induced graphene (LIG).

2.6.3. Fluorescence spectroscopy

The fluorescence properties of the laser-induced graphene (LIG) surface were evaluated using a BioTek fluorescence microplate reader. The LIG electrode was placed at the bottom of a 96-well microplate, and 100 μL of ultrapure water was added to each well. Fluorescence emission spectra were recorded using a fixed excitation wavelength of 410 nm, while the emission was scanned from 445 to 700 nm with 10 nm intervals. The obtained spectra were used to evaluate the intrinsic fluorescence characteristics of the fabricated LIG surface.

2.7. Cell lines and culture conditions

Human lung carcinoma (A549) and human cervical cancer (HeLa) cell lines were cultured under standard conditions. Cells were maintained in Dulbecco's Modified Eagle Medium (DMEM) supplemented with 10% (v/v) fetal bovine serum (FBS) and 1% (v/v) penicillin–streptomycin (P/S). Cultures were incubated at 37 °C in a humidified atmosphere containing 5% CO_2.

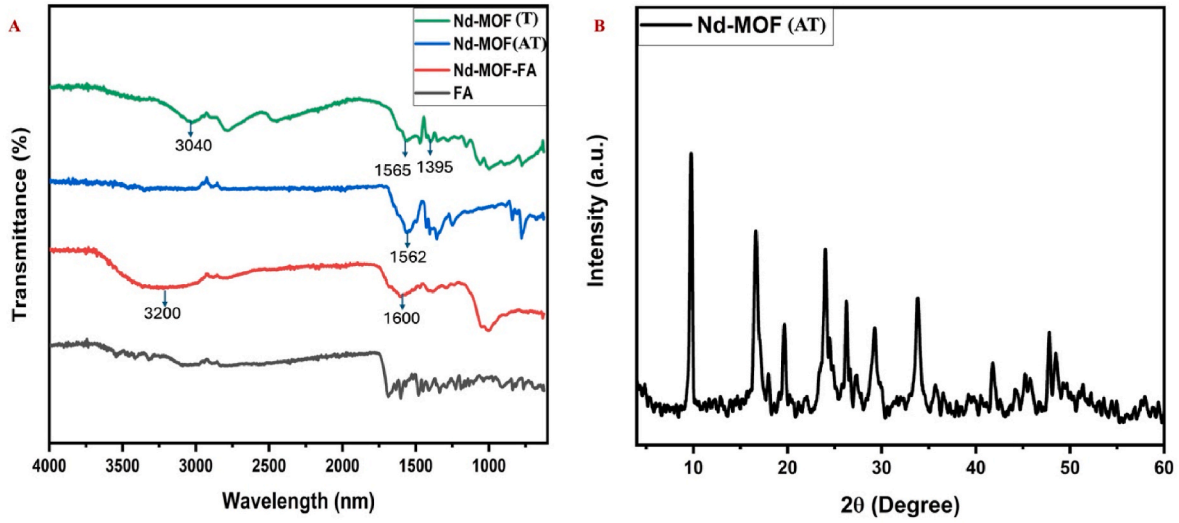


Fig. 1. (A) FTIR spectra of Nd-MOF, Nd-MOF-NH_2, Nd-MOF-FA, and folic acid (FA), confirming successful functionalization and amide bond formation. (B) XRD pattern of Nd-MOF, indicating high crystallinity and phase purity of the synthesized framework. T and AT denote terephthalic acid and 2-aminoterephthalic acid, respectively. The comparison between Nd-MOF (T) and Nd-MOF (AT) was included to highlight the effect of amino functionalization in the FTIR spectra. Since only Nd-MOF (AT) was used throughout the biosensor fabrication and all subsequent experiments, it is hereafter referred to as Nd-MOF throughout the remainder of the manuscript.

2.7.1. Cell proliferation analysis

Cell proliferation on coated surfaces was evaluated over time using the MTT assay. Cells were seeded onto modified surfaces and incubated under standard conditions. Proliferation was assessed at multiple time points, including 1, 24, 48, 72, and 96 h. At each time point, MTT reagent was added, and the assay was performed [16]. For this, TCPS, Gr, Gr/Nd-MOF and Gr/Nd-MOF-FA plates were placed in the wells, followed by the addition of 110 μL of 10% MTT solution (5.0 mg mL 1 PBS) per well and incubation for 4 h. Subsequently, 100 μL of SDS solution (1.0 g SDS in 10 mL 0.01 m HCl) was added, and after 24 h of incubation, the UV-visible absorption at 570 nm with 630 nm as the reference wavelength was measured using a microplate reader (Thermo Scientific Multiscan GO).

2.7.2. Fluorescence imaging

Cell adhesion and attachment behavior on modified surfaces were evaluated by fluorescence staining. A549 and HeLa cells were cultured on Gr, Gr/Nd-MOF, and Gr/Nd-MOF-FA modified surfaces for 48 h under standard conditions. Following incubation, cells were fixed and stained with 4′,6-diamidino-2-phenylindole (DAPI) solution (1.0 mg mL^{-1}) at 37 °C for 15 min to visualize cell nuclei. After staining, cells were washed three times with PBS to remove excess dye.

A549 and HeLa cells were cultured on Gr, Gr/Nd-MOF, and Gr/Nd-MOF-FA modified surfaces for 48 h under standard conditions. Following incubation, the cells were first stained with non-specific fluorescein isothiocyanate (FITC) for 2 h to visualize the cytoplasmic regions and overall cell morphology. Subsequently, the cells were fixed and stained with 4′,6-diamidino-2-phenylindole (DAPI, 1.0 mg mL^{-1}) at 37 °C for 15 min to visualize the nuclei. Fluorescence images were acquired using a Leica DM4000 B fluorescence microscope equipped with appropriate filter sets for both FITC and DAPI. The obtained images were qualitatively analyzed in terms of cell distribution, adhesion, morphology, and surface coverage to evaluate the interactions between the cells and the different material surfaces.

2.8. Cell sensor application

For electrochemical characterization and cell adhesion studies, a redox probe solution consisting of 5 mM $[Fe(CN)_6]^{3-/4-}$ and 0.1 M KCl (HCF solution) was used. LIG electrodes were directly fabricated on polyimide substrates via Diode laser scribing and used as the working electrodes, providing a highly porous and conductive surface. The Nd-MOF-FA structures were immobilized onto the graphene surface of the LIG electrode, resulting in the final sensing interface denoted as Gr/Nd-MOF-FA. To evaluate cell adhesion and targeting performance, folate receptor-positive HeLa cells and folate receptor-deficient A549 cells were used as model systems. A volume of 10 μL of cell suspension containing varying cell densities (5–7000 cells) was deposited onto the modified electrode surface and incubated for 30 min to allow cell attachment. After incubation, the electrode surfaces (Gr/Nd-MOF-FA/HeLa and Gr/Nd-MOF-FA/A549) were gently rinsed with 100 μL of deionized water to remove non-adherent cells. Subsequently, the HCF solution was applied onto the electrode surface, and differential pulse voltammetry (DPV) measurements were performed (Palmsens 4 potentiometer, driven by PSTrace 5.9 software was used for electrochemical measurements). The variation in DPV peak current before (I_o) and after cell interaction (I) was defined as the sensor response and mathematically expressed as Biosensor response (%) = $(I_o\text{-}I/I_o)*100$. Calibration curves of sensor response versus cell number were constructed for HeLa cell line to evaluate sensitivity and selectivity. Due to FA functionalization, enhanced binding affinity was observed toward HeLa cells, which overexpress folate receptors, whereas minimal interaction was observed with A549 cells. Electrochemical characterization of the modified electrodes was further carried out using cyclic voltammetry (CV) and electrochemical impedance spectroscopy (EIS). CV measurements were performed in the potential range of −0.4 to 0.8 V in a solution containing 5.0 mM $[Fe(CN)_6]^{3-/4-}$ and 0.1 M KCl. EIS measurements were conducted in 50 mM sodium phosphate buffer (pH 7.4) containing 5.0 mM $[Fe(CN)_6]^{3-/4-}$ and 0.1 M KCl, over a frequency range of 0.01–1000 Hz with an applied potential of 0.18 V.

The limit of detection (LOD) was statistically calculated using the standard IUPAC formula:

$$LOD = 3 \times \sigma / S$$

where σ is the standard deviation of ten independent measurements (n = 10) of the blank signal (i.e., the modified Gr/Nd-MOF-FA electrode in 5.0 mM $[Fe(CN)_6]^{3-/4-}$ solution without target cells), and S is the slope of the linear calibration plot in the range of 100–4000 cells.

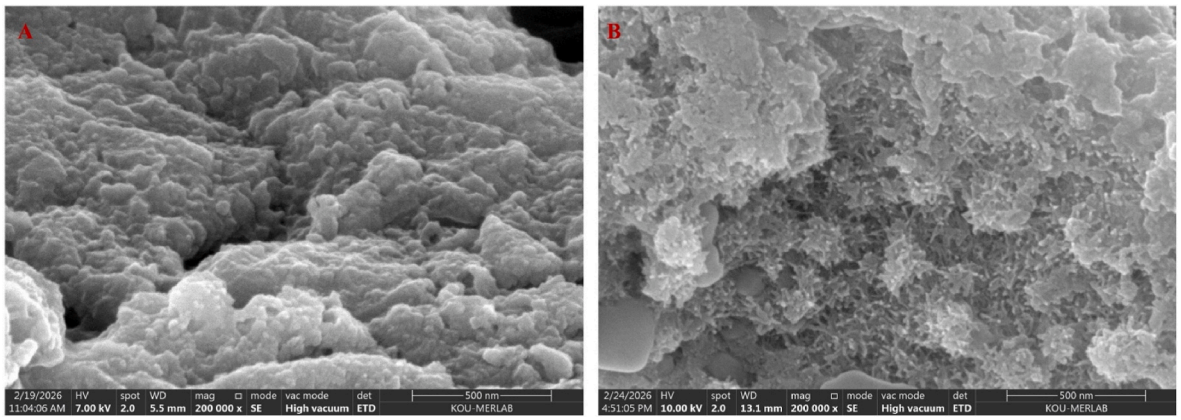


Fig. 2. Scanning electron microscopy (SEM) images of (A) pristine Nd-MOF and (B) folic acid-functionalized Nd-MOF (Nd-MOF-FA). The pristine Nd-MOF structure (A) exhibits a relatively dense and aggregated morphology, while folic acid modification (B) leads to a more heterogeneous and textured surface with increased surface roughness, indicating successful functionalization and structural alteration at the nanoscale.

2.9. Statistical analyses

The data are presented as the mean ± standard deviation (SD). Statistical analyses were conducted using one-way ANOVA, followed by Tukey's post-hoc test for multiple comparisons, utilizing GraphPad Prism 9 software. A p-value of <0.05 was considered statistically significant. The sample size is denoted by *n*.

3. Results and discussion

3.1. Characterization

The conjugation efficiency of folic acid was determined by UV–Vis spectroscopy using a calibration curve constructed from standard folic acid solutions. The calibration equation was $Y = 457.7X + 0.09537$, and the conjugation efficiency was calculated from the residual concentration of unconjugated folic acid remaining in the supernatant after conjugation. Based on this analysis, the folic acid conjugation efficiency was determined to be 95.62%. The chemical structures and successful functionalization of Nd-based MOF systems were evaluated by FTIR spectroscopy, as presented in Fig. 1A. The spectra correspond to pristine Nd-MOF, amine-functionalized Nd-MOF (Nd-MOF-NH_2), folic acid-conjugated Nd-MOF (Nd-MOF-FA), and pure folic acid (FA), enabling comparative analysis of functional group transformations.

For the pristine Nd-MOF, characteristic absorption bands were observed in the region of 1620–1550 cm^{-1} and 1400–1380 cm^{-1}, corresponding to the asymmetric and symmetric stretching vibrations of coordinated carboxylate groups ($–COO^-$) derived from terephthalic acid [17]. The absence of a sharp peak around ~1700 cm^{-1} (free –COOH) confirms successful coordination between neodymium ions and the organic linker, consistent with typical MOF formation [18]. Additionally, broad bands observed around 3000–3500 cm^{-1} can be attributed to O–H stretching vibrations [19], likely arising from adsorbed water molecules or hydroxyl groups within the MOF structure.

In the case of Nd-MOF-NH_2, the spectrum shows additional features associated with amine functionalization. The appearance of bands around near ~1650–1540 cm^{-1} can be assigned to C-N and NH_2 bending modes [3]. These observations confirm the successful incorporation of amino-functionalized terephthalic acid into the MOF framework. The preservation of carboxylate-related peaks further indicates that the coordination environment of the MOF structure remains intact after functionalization.

The FTIR spectrum of Nd-MOF-FA reveals significant changes compared to Nd-MOF-NH_2, indicating successful conjugation of folic acid. Notably, the emergence of a characteristic amide bond is supported by the presence of amide I and amide II bands around ~1600–1800 $cm^{-1}$and ~1470–1570 cm^{-1}, respectively [20] These peaks arise from C=O stretching (amide I) and N–H bending/C–N stretching (amide II), confirming the formation of a covalent linkage between folic acid and the amine-functionalized MOF. The broadening of peaks in the 3000–3500 cm^{-1} region further reflects overlapping O–H stretching modes [19], consistent with the presence of multiple functional groups in folic acid.

Overall, the FTIR results clearly demonstrate the successful synthesis and stepwise functionalization of the Nd-based MOF system. The preservation of MOF-specific carboxylate coordination peaks, combined with the appearance of amine-related bands in Nd-MOF-NH_2 and amide bond signatures in Nd-MOF-FA, confirms the effective conjugation of folic acid onto the MOF surface. These findings provide strong evidence for the successful construction of a biofunctionalized MOF platform, which is essential for subsequent biological and targeting applications.

The crystalline structure of the synthesized Nd-MOF was analyzed by X-ray diffraction (XRD), as presented in Fig. 1B. The diffraction pattern exhibits a series of sharp and well-defined peaks, indicating a highly crystalline framework. The presence of intense reflections confirms the successful formation of an ordered metal–organic framework structure rather than an amorphous phase. The observed diffraction pattern is consistent with previously reported rare-earth-based MOFs, where characteristic peaks in the low-to-mid 2θ range (7–20°) correspond to the framework topology and metal–ligand coordination geometry. The obtained XRD results are in good agreement with previously reported patterns, particularly those described by Karaca et al. (2025) [21] for MOFs synthesized using terephthalic acid and gadolinium(III) chloride hexahydrate, as well as by Luo et al. (2017) [22] for neodymium-based MOFs constructed with aminoterephthalic acid, confirming the consistency of the crystalline structure. Minor variations in peak positions and intensities may arise from differences in synthesis conditions, solvent incorporation, or coordination environment.

The Raman spectrum of the LIG surface exhibits the characteristic D (~1350 cm^{-1}) and G (~1580 cm^{-1}) bands, confirming the formation of a graphene-based composite structure. The prominent D band indicates the presence of structural defects and edge sites generated during the laser-induced graphitization process, whereas the G band corresponds to the graphitic sp^2 carbon network. These results support the successful formation of the laser-induced graphene composite on the electrode surface (Fig. S1).

The surface morphologies of pristine, non-immobilized Nd-MOF and folic acid-functionalized Nd-MOF (Nd-MOF-FA) structures are presented in Fig. 2. The pristine MOF (Fig. 2A) exhibits a dense and aggregated particulate morphology, indicating a compact surface architecture formed by closely packed MOF crystals. In contrast, the folic acid-functionalized MOF (Nd-MOF-FA) (Fig. 2B) shows a pronounced

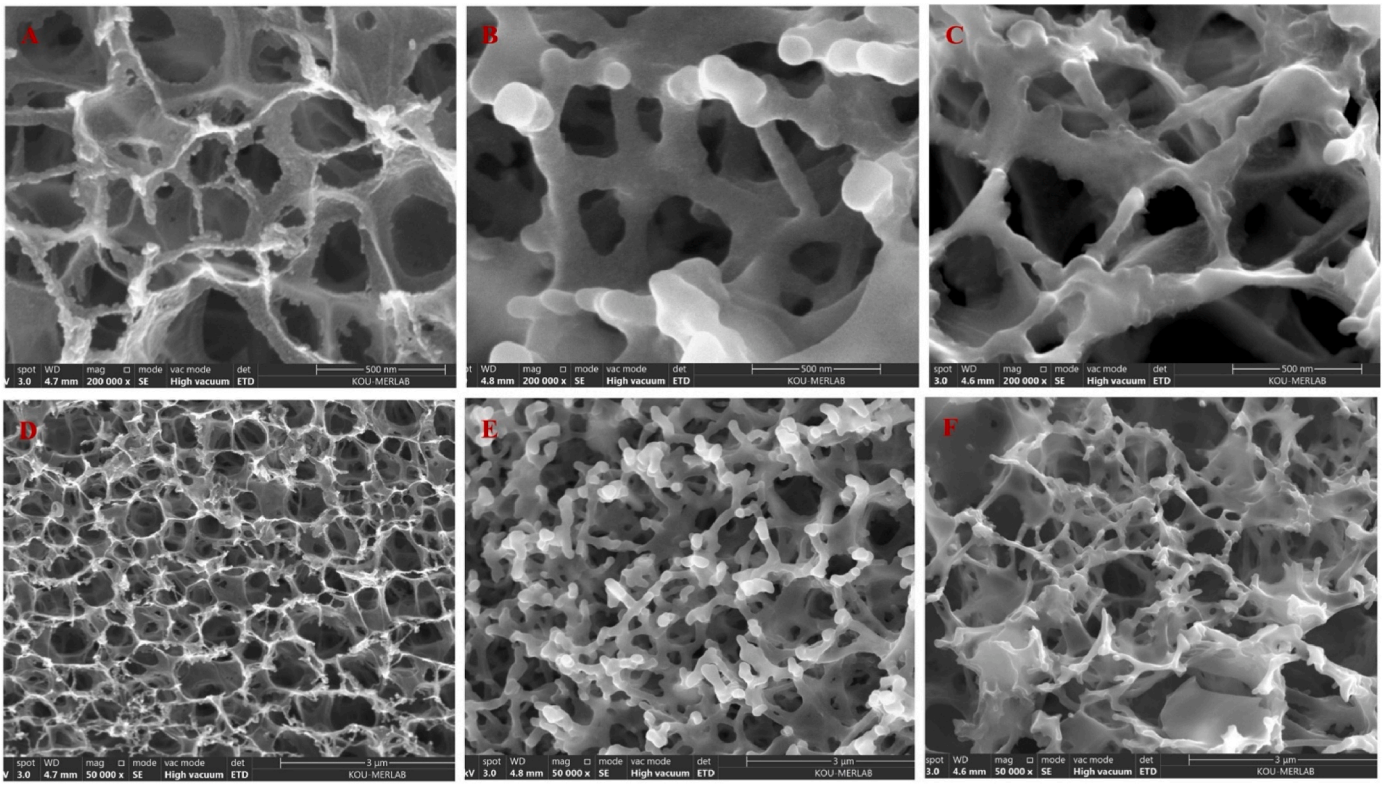


Fig. 3. Scanning electron microscopy (SEM) images of (A) graphene (Gr), (B) graphene-MOF (Gr/Nd-MOF), and (C) folic acid-functionalized graphene-MOF (Gr/Nd-MOF-FA) surfaces (scala bar 500 nm). Images (D–F) represent the corresponding morphologies at lower magnification (scale bar 3 μm), illustrating the overall porous architecture and surface topology. The Gr structure (A, D) exhibits a typical interconnected porous network, while Gr/Nd-MOF (B, E) shows increased surface roughness and particle-like features due to Nd-MOF incorporation. Functionalization with folic acid (C, F) results in a more uniform and interconnected morphology, suggesting successful surface modification.

morphological transformation, characterized by a more heterogeneous and roughened surface. The increase in surface roughness and irregular topography suggests the successful conjugation of folic acid molecules onto the MOF framework, leading to nanoscale structural modifications. It has been widely reported that functionalization processes can significantly alter the morphology and surface energy of MOFs, thereby directly influencing their biological interactions [23,24].

SEM images of graphene (Gr), graphene/Nd-MOF (Gr/Nd-MOF), and folic acid-functionalized graphene-MOF (Gr/Nd-MOF-FA) surfaces further highlight the structural differences among the materials (Fig. 3). Also, Elemental mapping analysis performed by EDS (Fig. S2) demonstrated a homogeneous distribution of the constituent elements across the modified surface, confirming the uniform formation of the composite layer. The pristine graphene surface (Fig. 3-A, D) displays a characteristic three-dimensional, interconnected porous network, which is typical of LIG. This architecture provides a high surface area and excellent electrical conductivity, making it highly suitable for electrochemical applications [24,25].

Upon integration of Nd-MOF onto the graphene surface, the resulting Gr/Nd-MOF structure (Fig. 3-B, E) exhibits a notable change in surface topology, with the emergence of particle-like features distributed across the graphene matrix. This observation indicates that Nd-MOF crystals are successfully immobilized onto the graphene surface through a self-assembly process [26,27]. Although the overall porous structure is partially preserved, the surface evolves into a more complex and hierarchically organized morphology. Such hybrid structures provide both high surface area and abundant functional active sites, which are advantageous for sensing and biomedical applications [28].

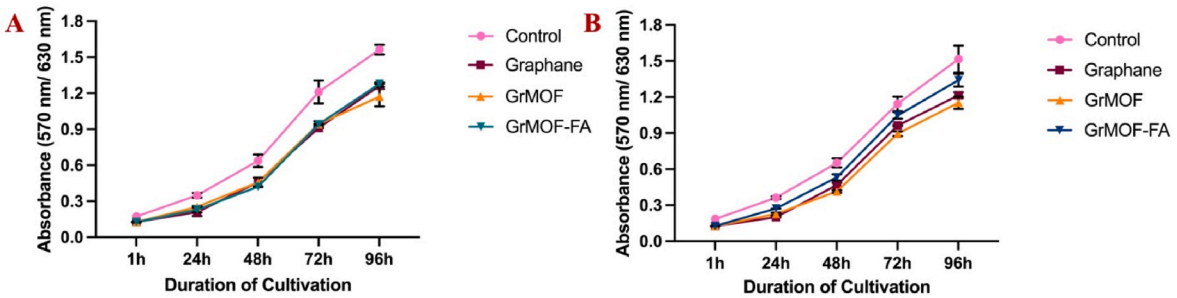


Fig. 4. Cell proliferation analysis of A549 cells (A) and HeLa cells (B) cultured on different material surfaces over time. Cells were incubated with LIG, graphene-MOF (Gr/Nd-MOF), and folic acid-functionalized graphene-MOF (Gr/Nd-MOF-FA), and proliferation was assessed at 1, 24, 48, 72 and 96 h using absorbance measurements (570 nm/630 nm). The control group represents cells cultured without material exposure. All groups exhibited time-dependent increases in proliferation; however, material-treated groups showed slightly reduced proliferation compared to control, with Gr/Nd-MOF-FA demonstrating relatively improved cell growth compared to Gr/Nd-MOF alone. Data are presented as mean ± SD.

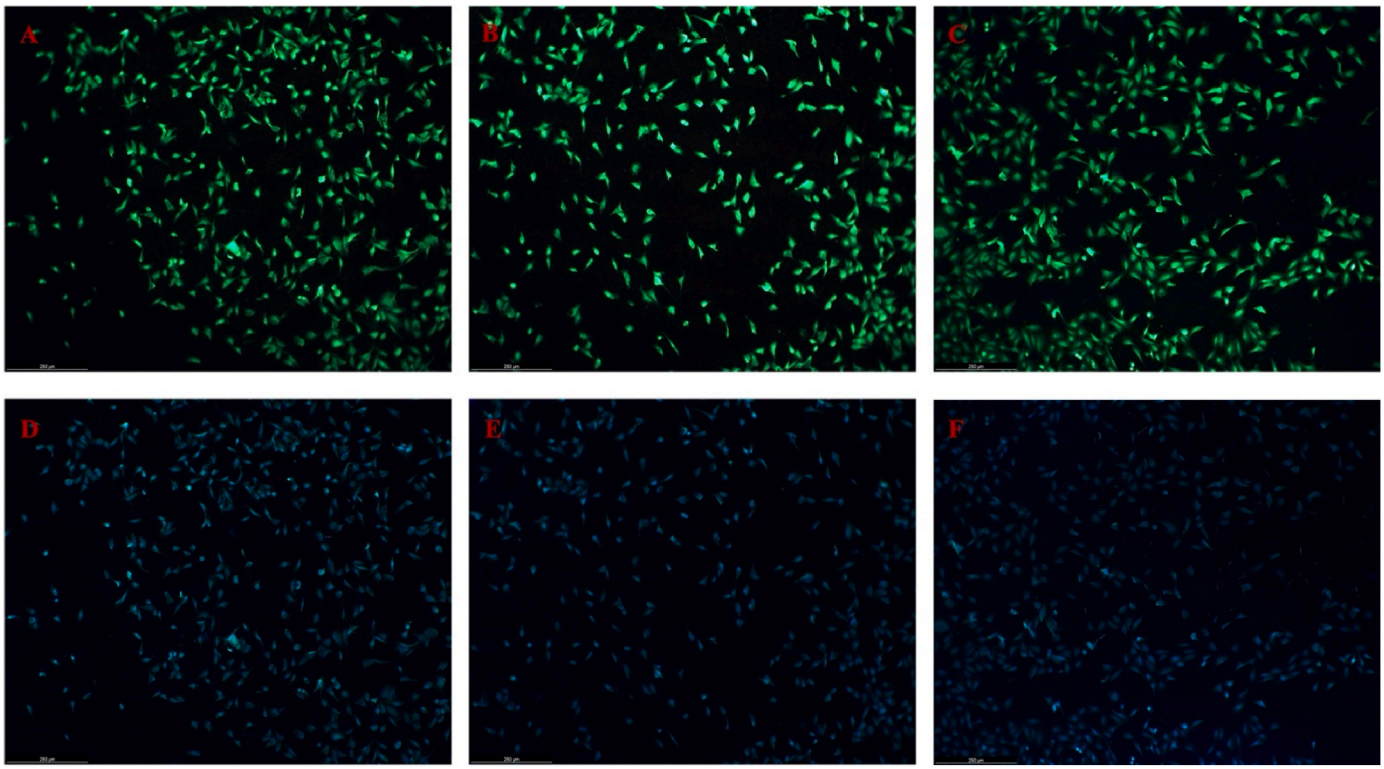


Fig. 5. Non-specific FITC staining was used to visualize cell density and morphology of the A549 cells cultured on different surfaces. (A) LIG surface, (B) Gr/Nd-MOF, and (C) Gr/Nd-MOF-FA. Corresponding nuclear staining images using DAPI staining are shown in (D), (E), and (F), respectively. FITC images (A–C) indicate relative cell density and spreading, while DAPI images (D–F) confirm nuclear distribution and cell population across the different material surfaces.

For the folic acid-functionalized Gr/Nd-MOF-FA surfaces (Fig. 3-C, F), a more compact and interconnected morphology is observed, with partial closure of the pores. This suggests that folic acid does not merely act as a passive surface modifier, but also influences the structural organization, leading to a more uniform distribution of the composite components. Lower magnification images (Fig. 3-D–F) confirm that the overall porous architecture is retained across all samples; however, Gr/Nd-MOF and particularly Gr/Nd-MOF-FA exhibit a more continuous and organized network structure.

These morphological changes are critically important for cell–material interactions. Increased surface roughness and heterogeneity are known to enhance cell adhesion, whereas more uniform and interconnected structures support improved cell spreading and proliferation [29]. In this context, the improved structural organization observed in Gr/Nd-MOF-FA surfaces correlates well with the proliferation results, indicating enhanced cellular behavior on these substrates.

In conclusion, SEM analyses clearly demonstrate that both Nd-MOF incorporation and folic acid functionalization significantly modify the surface morphology. While Nd-MOF integration increases surface roughness and functional complexity, folic acid modification leads to a more organized and biologically favorable interface. These structural characteristics highlight the potential of the developed system as a tunable platform for optimizing both electrochemical performance and biological interactions.

3.2. Cell culture experiments

The cell proliferation profiles of A549 and HeLa cells cultured on LIG-based and modified surfaces are presented in Fig. 4. In both cell lines, a clear time-dependent increase in absorbance values was observed over the 96-h incubation period, indicating sustained cellular growth and viability across all experimental groups. This trend confirms that none of the tested materials exhibited acute cytotoxic effects under the experimental conditions, which is consistent with previous studies demonstrating the general biocompatibility of graphene-based substrates in cancer cell cultures [30,31].

Despite the overall increase in proliferation, a slight but consistent reduction in cell growth was observed in all material-treated groups compared to the control. This effect was more pronounced in the Gr/Nd-MOF group, suggesting that the incorporation of Nd-MOF structures onto the graphene surface may introduce mild inhibitory effects on cell proliferation. This phenomenon can be attributed to several factors, including increased surface roughness, altered surface charge, and potential ion release from MOF components, which are known to influence cell–material interactions [32,33]. In particular, MOF-derived metal ions and coordination environments may modulate cellular adhesion dynamics, thereby slightly suppressing proliferation rates.

Interestingly, the folic acid-functionalized Gr/Nd-MOF-FA surfaces demonstrated relatively improved cell proliferation compared to Gr/Nd-MOF alone, although still lower than the control. This enhancement can be explained by the well-established role of folic acid in facilitating receptor-mediated cellular interactions. Many cancer cell lines, including HeLa, overexpress folate receptors, which enables enhanced binding and uptake of folic acid-modified materials [34,35].The presence of folic acid likely promotes more favorable cell adhesion and interaction with the substrate, partially compensating for the inhibitory effects introduced by the Nd-MOF structure.

Overall, these findings demonstrate that while graphene and its composites slightly modulate cell proliferation, they maintain a favorable biological profile. The incorporation of Nd-MOF structures introduces tunable bio-interfacial properties, and folic acid functionalization effectively enhances cellular compatibility through receptor-mediated mechanisms.

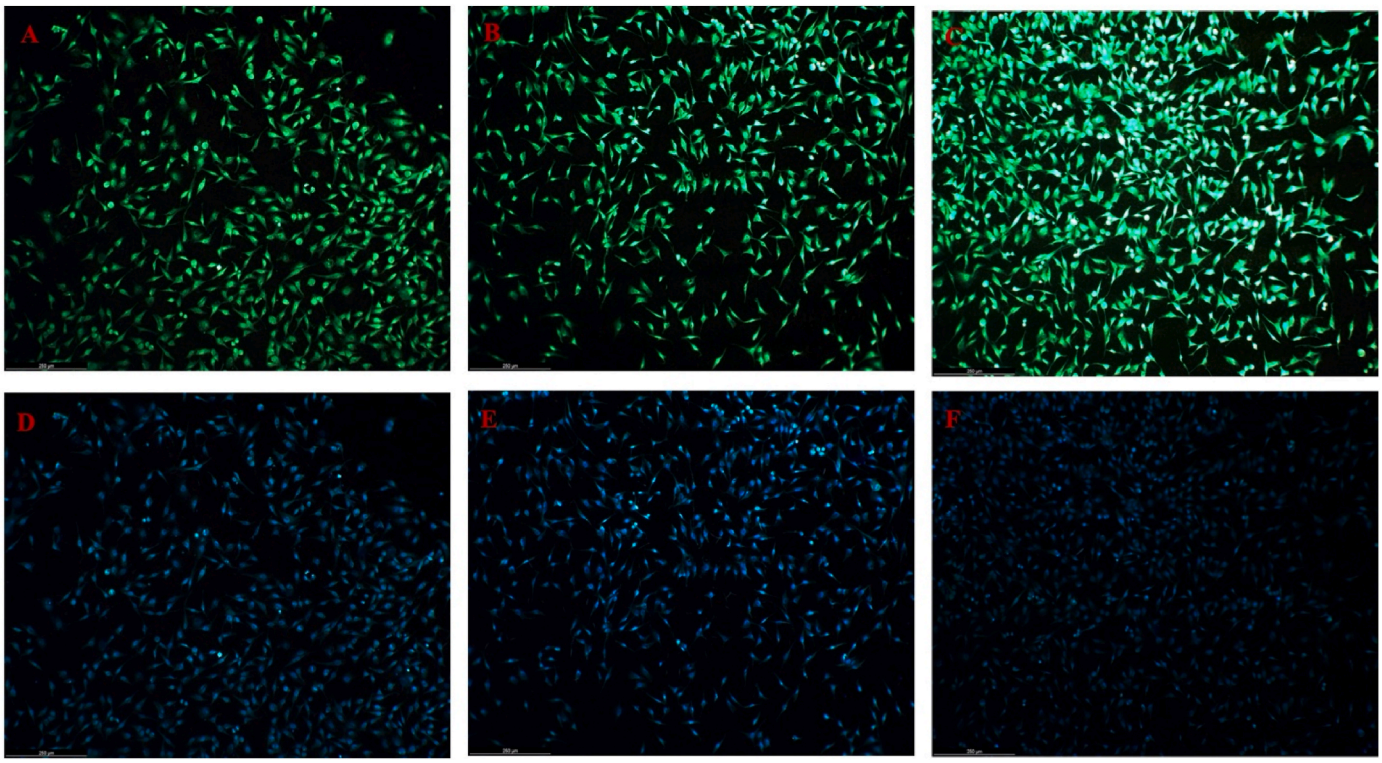


Fig. 6. Non-specific FITC staining was used to visualize cell density and morphology of the HeLa cells cultured on different surfaces. (A) Gr surface, (B) Gr/Nd-MOF, and (C) Gr/Nd-MOF-FA. Corresponding nuclear staining images using DAPI staining are shown in (D), (E) and (F), respectively. FITC images (A–C) indicate relative cell density and spreading, while DAPI images (D–F) confirm nuclear distribution and cell population across the different material surfaces.

3.3. Fluorescence microscopy

Fluorescence imaging was performed to evaluate cell density, morphology, and surface interactions of A549 and HeLa cells cultured on graphene-based substrates, and the results are presented in Figs. 5 and 6. Non-specific FITC staining (Figs. 5 and 6 A–C) was used to visualize overall cell distribution and morphology, while DAPI staining (Figs. 5 and 6 D–F) enabled assessment of nuclear localization and cell population across the different material surfaces.

For A549 cells (Fig. 5), the Gr surface (A, D) exhibited a homogeneous cell distribution and well-spread morphology, indicating favorable cell adhesion and biocompatibility. In contrast, the Gr/nd-MOF surface (B, E) showed a noticeable reduction in cell density and spreading, with cells appearing more sparsely distributed and less organized. This behavior suggests that the increased surface heterogeneity and altered physicochemical properties resulting from Nd-MOF integration may negatively affect cell adhesion and cytoskeletal organization. It has been reported that surface roughness and compositional complexity can significantly influence protein adsorption and subsequent cell attachment behavior [36]. In contrast, Gr/Nd-MOF-FA surface (C, F) demonstrated a marked improvement compared to the Gr/Nd-MOF group. Cells appeared more densely and homogeneously distributed, with enhanced spreading and more pronounced cytoskeletal features. DAPI staining further confirmed a higher number of nuclei, supporting increased cell attachment and proliferation. This improvement can be attributed to the formation of a more homogeneous surface due to partial pore filling by folic acid, as well as enhanced cell–surface interactions mediated by folic acid functionalization.

Similar trends were observed for HeLa cells (Fig. 6). While the Gr surface (A, D) supported good cell adhesion and distribution, the Gr/Nd-MOF surface (B, E) exhibited reduced cell density and less organized morphology. In contrast, the Gr/Nd-MOF-FA surface (C, F) showed a significant increase in cell density, along with a more spread and organized cellular morphology. The high expression of folate receptors in HeLa cells likely contributes to the improved cellular response observed on Gr/Nd-MOF-FA surfaces.

Overall, the fluorescence imaging results for both cell lines consistently demonstrate that Nd-MOF integration slightly suppresses cell adhesion and spreading, whereas folic acid functionalization effectively reverses this effect and significantly enhances cell–material interactions [37,38]. These findings are in strong agreement with SEM and proliferation data, highlighting the critical role of surface chemistry and morphology in regulating biological responses. The improved cellular behavior observed on Gr/Nd-MOF-FA surfaces suggests that these systems provide a suitable and effective biointerface for applications in biosensing and imaging platforms.

The surface morphology and laser-induced optical properties of the graphene-modified substrates were investigated using SEM and fluorescence imaging, as presented in Fig. 7. The SEM image (Fig. 7A) reveals a well-defined, patterned surface morphology characteristic of LIG, exhibiting aligned microstructures and a relatively roughened topology. Such features are known to arise from localized photothermal conversion during laser irradiation, leading to the formation of porous and conductive graphene domains.

During fluorescence imaging under the DAPI filter (Fig. 7B), an unexpected red stripe-like background signal was observed while imaging cells on the graphene-modified surface. This raised the question of whether the observed red emission originated from DAPI staining or from intrinsic optical properties of the LIG surface. To clarify this, control experiments were performed on graphene surfaces without any biological staining or treatment.

Fluorescence images acquired from untreated graphene surfaces fabricated under low and high laser intensities (Fig. 7-C–F) provide important insights into the origin of the observed signal. Under low laser intensity conditions (Fig. 7-C, D), weak and sparsely distributed fluorescence signals were detected, suggesting limited formation of emissive structures. In contrast, graphene surfaces produced under higher laser intensity (Fig. 7-E, F) exhibited significantly enhanced fluorescence

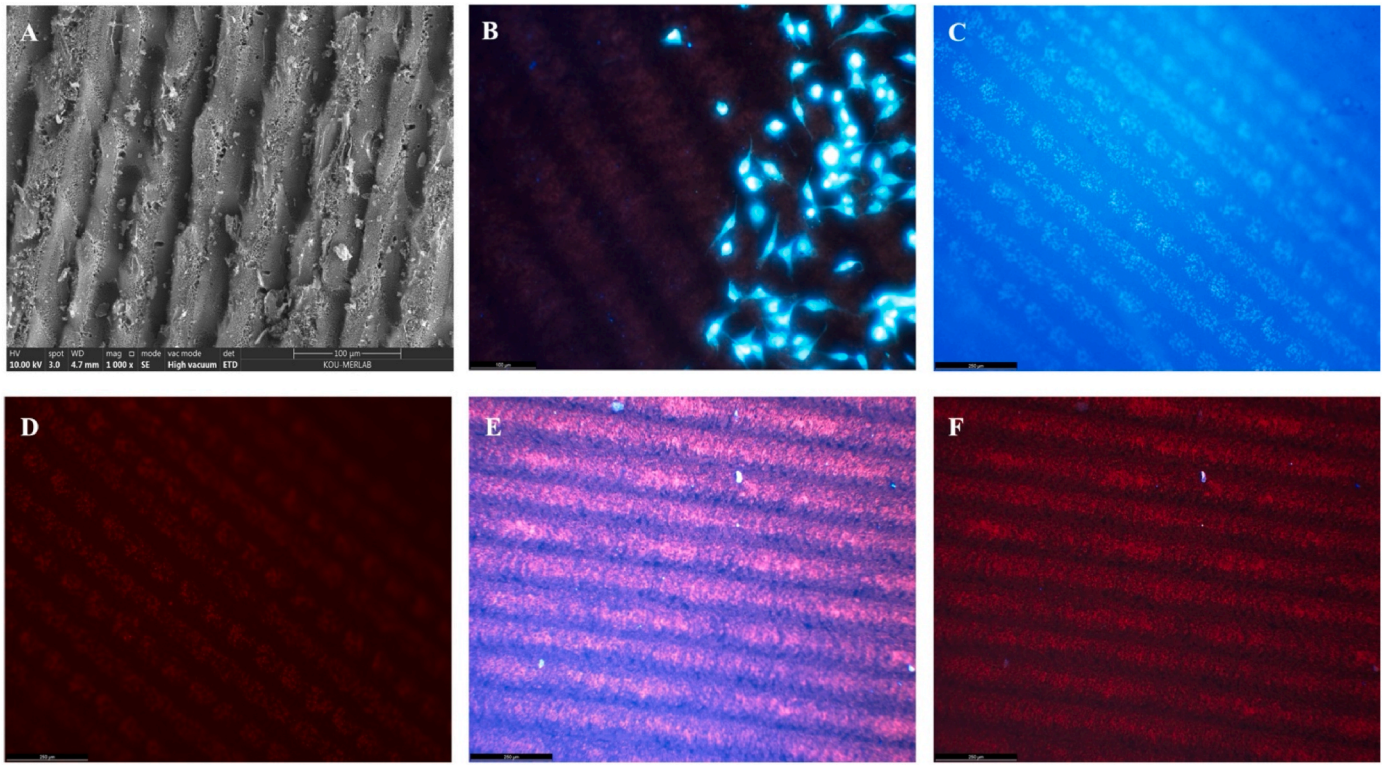


Fig. 7. (A) SEM image of the LIG surface showing the surface morphology (scale bar: 100 µm). (B) Fluorescence image acquired under DAPI filter, where background reflection appears as red stripe-like patterns (scale bar: 100 µm). (C) Fluorescence image of graphene dots formed under low laser intensity, showing weak signal distribution under DAPI filter (scale bar: 250 µm). (D) Corresponding red-channel fluorescence image of graphene dots formed under low laser intensity (scale bar: 250 µm). (E) Fluorescence image of graphene dots generated under high laser intensity, indicating enhanced signal and more uniform distribution under DAPI filter (scale bar: 250 µm). (F) Red-channel fluorescence image of graphene dots formed under high laser intensity, demonstrating increased fluorescence intensity and surface coverage (scale bar: 250 µm).

intensity and more uniform signal distribution across the surface (all experiments in this study were performed on graphene surfaces fabricated under high laser intensity conditions).

Importantly, these fluorescence signals were observed under both DAPI and red filters in the absence of any staining agents, confirming that the emission is not related to DAPI but rather originates from the intrinsic properties of the LIG structures. The observed emission can be attributed to the formation of graphene nanodots [27,39] or defect-rich carbon domains, which are known to exhibit fluorescence due to quantum confinement effects and surface defect states [40,41]. The increased laser intensity likely promotes the formation of more uniform and densely distributed graphene composite, resulting in stronger and more homogeneous fluorescence signals.

Furthermore, the homogeneous distribution of fluorescence observed in Fig. 7-C–F indicates that the laser processing parameters play a critical role in controlling the optical properties of the graphene surface. The ability to tune fluorescence intensity and distribution through laser power provides a versatile approach for engineering optically active graphene-based platforms.

Overall, these findings demonstrate that the observed red emission during fluorescence imaging is an inherent property of the LIG surface rather than an artifact of DAPI staining. Moreover, the formation of uniformly distributed, fluorescence-active graphene composite highlights the strong potential of these surfaces for the development of fluorescence-based sensing platforms, particularly in the design of sensitive and tunable fluorescence sensors. To further characterize the optical properties of the LIG surface, fluorescence emission spectroscopy was performed (Fig. S3). The fluorescence spectrum exhibited a pronounced emission peak in the blue region together with a broad emission profile extending toward the red region, indicating the intrinsic fluorescence behavior of the laser-induced graphene composite While graphene nanodots are typically synthesized in liquid-phase systems in the literature, the present approach enables their direct formation on solid surfaces, offering improved spatial control, patternability, and enhanced uniformity. This surface-confined synthesis strategy allows for more controlled and homogeneous potential nanodot distribution compared to conventional solution-based methods. Consequently, such precisely engineered fluorescent graphene surfaces hold significant promise for integration into advanced technological applications, ranging from microfluidic platforms to highly sensitive sensor systems.

3.4. Electrochemical characterization and cytosensing performance

The electrochemical behavior of the fabricated biosensor at each modification step was systematically investigated using cyclic voltammetry (CV) and electrochemical impedance spectroscopy (EIS). The electrode-to-electrode reproducibility of the fabricated LIG/Nd-MOF-FA biosensors was evaluated using six independently prepared electrodes fabricated under identical conditions. As shown in Fig. S4, the biosensor responses were highly consistent, indicating good fabrication reproducibility and reliable sensor performance. As shown in Fig. 8A, the bare graphene electrode (Gr) exhibits a well-defined and reversible redox response, indicating efficient electron transfer kinetics associated with its porous structure. Following modification with Nd-MOF-FA (Gr/Nd-MOF-FA), a decrease in peak current is observed, which can be attributed to the partially insulating nature of the organic framework that hinders electron transfer.

The selectivity of the cytosensor was evaluated using A549 and HeLa cell lines. After incubation with A549 cells, only a slight decrease in current is observed, which is attributed to weak non-specific adsorption. In contrast, incubation with HeLa cells results in a significant attenuation of the faradaic current, indicating strong and specific interaction

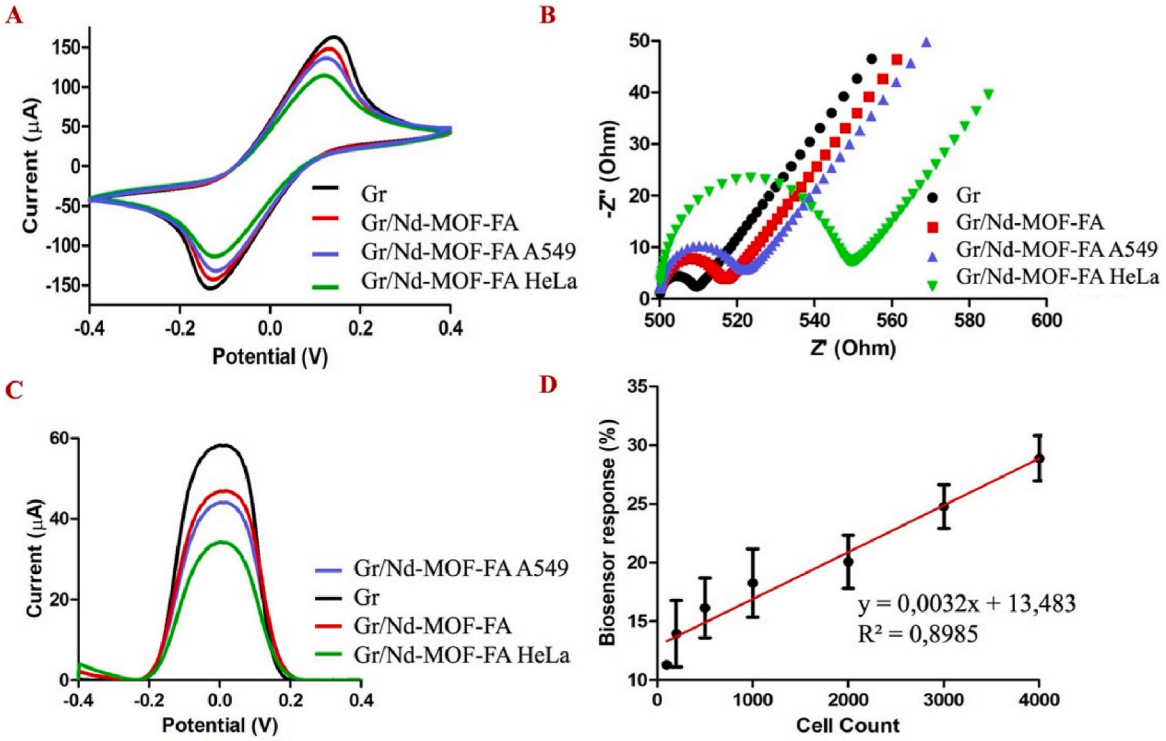


Fig. 8. Electrochemical characterization and biosensing performance of the developed Gr/Nd-MOF-FA platform. (A) Cyclic voltammetry (CV) responses of Gr, Gr/Nd-MOF-FA, and after interaction with A549 and HeLa cells, showing changes in redox peak currents upon cell attachment. (B) Electrochemical impedance spectroscopy (EIS) Nyquist plots of the corresponding surfaces, indicating variations in charge transfer resistance (Rct) following cell binding. (C) Differential pulse voltammetry (DPV) responses illustrating the decrease in peak current after interaction with A549 and HeLa cells, with a more pronounced effect observed for HeLa cells due to folate receptor-mediated binding. (D) Calibration curve of biosensor response (%) vs. HeLa cell count obtained via Differential Pulse Voltammetry (DPV) measurements, demonstrating a linear relationship. Data are presented as mean ± SD. All electrochemical and biological experiments were carried out using LIG electrodes fabricated under the optimized laser conditions described in the Materials and Methods section.

between folic acid moieties and folate receptors on the cell membrane. The captured HeLa cells form a steric barrier on the electrode surface, limiting the diffusion of the redox probe [42,43].

These observations are further supported by EIS measurements (Fig. 8B). The Nyquist plots reveal a gradual increase in charge transfer resistance (Rct) from Gr to Gr/Nd-MOF-FA, followed by a pronounced increase after cell incubation. Notably, the Rct value for HeLa cells is significantly higher than that for A549 cells, confirming selective cell capture and the formation of an insulating biological layer [44].

Differential pulse voltammetry (DPV) analysis (Fig. 8C) shows a similar trend. The highest current response is observed for the bare Gr electrode, while a decrease occurs after surface modification. Following incubation with A549 cells, only a minor signal change is detected, whereas a substantial decrease is observed for HeLa cells, further confirming receptor-mediated binding and steric hindrance effects [45,46].

The quantitative detection performance of the biosensor was evaluated by constructing a calibration curve based on biosensor response (%) versus HeLa cell count (Fig. 8D). A strong linear relationship is observed within the range of 100–4000 cells, indicating sensitive and reliable detection. Beyond this range, the response deviates from linearity and approaches a plateau, suggesting saturation of available binding sites on the electrode surface [47]. Additionally, increased variability at higher cell concentrations is attributed to non-specific cell stacking and unstable attachment, which can lead to signal fluctuations [48]. The quantitative calibration curve in Fig. 8D was constructed based on DPV peak current attenuation (Biosensor response (%) = (Io - I)/Io x 100) in the presence of varying concentrations of HeLa cells. While a minor signal change was recorded for A549 cells due to weak non-specific physical interactions with the porous composite interface, HeLa cells exhibited a distinctly stronger response driven by specific folate receptor-ligand interactions. To further boost selectivity for practical clinical applications, future iterations can incorporate antifouling surface coatings (e.g., PEGylation) or secondary blocking agents (e.g., BSA) to completely suppress non-specific background signals. The linear regression analysis of the calibration curve (Biosensor response (%) vs. HeLa cell count, Fig. 8D) yielded a slope (S) of 0.00396%/cell ($R^2 = 0.988$) over the concentration range of 100–4000 cells. Based on the standard deviation of 10 independent blank replicates ($\sigma = 0.81\%$), the limit of detection (LOD) was calculated to be 236 cells (using 3 x σ/S), providing statistical justification for the sensitive detection capability of the Gr/Nd-MOF-FA platform toward folate receptor-overexpressing cancer cells.

Although both EIS and DPV successfully monitored the interfacial changes associated with electrode modification and subsequent cell attachment, DPV was selected for quantitative analysis because of its higher signal-to-noise ratio, rapid measurement time, and straightforward data interpretation. Pulse modulation effectively suppresses non-faradaic capacitive currents, allowing sensitive detection of changes in the faradaic current of the $[Fe(CN)6]^{3-/4-}$ redox probe. In contrast, while EIS provides valuable information regarding interfacial charge-transfer resistance, quantitative analysis requires equivalent circuit fitting, which may introduce model-dependent variability. he consistency between the EIS and DPV results confirms that both techniques effectively reflect the interfacial changes occurring during sensor fabrication and cell recognition; however, DPV was preferred as the final quantitative method because of its higher analytical precision, shorter acquisition time, and greater suitability for future portable sensing applications. Overall, the results presented in Fig. 8 demonstrate that the Gr/Nd-MOF-FA platform enables highly selective and sensitive detection of folate receptor-positive HeLa cells through specific bio-

Table 1
Comparison of recently reported MOF-based electrochemical cytosensors for cancer cell detection and the proposed LIG/Nd-MOF-FA sensing platform.

Sensor Platform	Target Cell	Detection Method	Linear Range	LOD	Ref.
UiO-66-FA	HeLa and H1299	EIS	100-1.0 × 10^7	90	[49]
Nd-MOF nanorods	MCF-7	NIR photoelectrochemical	50–1.0 × 10^7	18	[50]
Cr-MOF	CT26	EIS/DPV	50–1 × 10^7	36	[51]
PCN-224	MCF-7	EIS/DPV	20–1 × 10^7	6	[52]
Hb-AgNCs@MOF-G	SKBR3, MCF-7, MDA-MB231	EIS	10^2–5 × 10^4	2	[53]
PNT–FA/graphene	HeLa	CV	2.5 × 102–5 × 103	250	[43]
CNTs@PDA-FA/GCE	HeLa	EIS	5 × 102– 1 × 106	500	[54]
Nd-MOF-FA	HeLa	EIS/DPV/Fluorescence	10^2–4×10^3	256	This work

recognition and steric blocking mechanisms.

Compared with previously reported electrochemical cytosensors, the proposed LIG/Nd-MOF-FA platform offers several practical advantages, including simple one-step laser fabrication, low-cost and scalable production, and dual-mode electrochemical (DPV) and fluorescence detection. The synergistic combination of LIG and Nd-MOF provides a conductive interface with a large active surface area, while folic acid functionalization enables selective recognition of FR-overexpressing HeLa cells over FR-low A549 cells. Beyond cancer cell detection, the platform allows real-time monitoring of cell behavior and may serve as a rapid alternative to conventional colorimetric assays, such as the MTT assay, as well as a versatile platform for evaluating future theranostic materials, including fluorescent polymers and nanoparticles (Table 1).''

4. Conclusion

In this study, a multifunctional electrochemical biosensing platform was successfully developed by integrating LIG with neodymium-based metal–organic frameworks (Nd-MOFs) and subsequent folic acid (FA) functionalization. Structural and chemical analyses (FTIR, XRD, SEM) confirmed the successful synthesis of the Nd-MOF, preservation of its crystalline framework, and effective conjugation of FA via amide bond formation. The incorporation of Nd-MOF onto the graphene surface enhanced surface roughness and functional active sites, while FA modification improved surface homogeneity and biointerface compatibility.

Electrochemical characterization using CV, DPV, and EIS verified the successful stepwise modification of the electrode surface and demonstrated its sensitive electrochemical response toward cancer cell detection. The developed biosensor exhibited selective recognition toward folate receptor-positive HeLa cells, achieving a limit of detection (LOD) of 236 cells, while showing minimal response to A549 cells. Cell proliferation and fluorescence imaging studies further confirmed that FA functionalization enhances cell adhesion and targeting efficiency without inducing cytotoxic effects. Additionally, the LIG surfaces exhibited intrinsic fluorescence behavior attributed to the formation of graphene composite, enabling dual electrochemical and optical functionality. Unlike conventional liquid-phase synthesis, the direct formation of these nanostructures on the surface allows improved control, uniformity, and patternability. Overall, this study presents a multifunctional and highly sensitive biosensing platform that combines electrochemical and optical features. The proposed platform may serve as a versatile tool for evaluating for future investigations into cancer cell detection, cell monitoring, and other biomedical applications, including diagnostic and theranostic strategies. Beyond proof-of-concept cell detection, the proposed platform could potentially be applied to patient-derived biopsy or liquid biopsy samples. Furthermore, integration into multiplexed microarray-based systems may enable simultaneous profiling of multiple cancer-associated surface receptors and cellular characteristics, providing valuable information for biomarker evaluation and personalized treatment strategies in precision oncology.

Declaration of competing interest

The authors declare that they have no known competing financial interests or personal relationships that could have appeared to influence the work reported in this paper.

Acknowledgements

This study was supported by the Scientific and Technological Research Council of Türkiye (TÜBİTAK) under the 2210-C Scholarship Program (Grant No: 1649B022406287). Additional financial support was provided by the Scientific Research Projects Coordination Unit of Istanbul University-Cerrahpaşa (BAP) (Project No: FBA-2025-38465).

The authors acknowledge the use of ChatGPT-5.2 for language editing and preliminary drafting. All generated content was critically reviewed and revised by the authors, who take full responsibility for the final version of the manuscript. Some schematic elements in the graphical abstract were generated using Gemini AI and subsequently integrated and finalized in Microsoft PowerPoint.

Appendix A. Supplementary data

Supplementary data to this article can be found online at https://doi.org/10.1016/j.mtnano.2026.100945.

Data availability

Data will be made available on request.

References

[1] H.-C. Zhou, J.R. Long, O.M. Yaghi, Introduction to metal–organic frameworks, Chem Rev 112 (2012) 673–674.
[2] K. Patra, H. Pal, Lanthanide-based metal–organic frameworks (Ln-MOFs): synthesis, properties and applications, RSC Sustain. 3 (2025) 629–660.
[3] X. Yuan, K. Luo, K. Zhang, J. He, Y. Zhao, D. Yu, Combinatorial vibration-mode assignment for the FTIR spectrum of crystalline melamine: a strategic approach toward theoretical IR vibrational calculations of triazine-based compounds, J. Phys. Chem. A 120 (2016) 7427–7433.
[4] S. Feng, W. Ding, Y. Zhang, J. Wu, Z. Zou, T. Wu, Q. Tang, A nanoscale Nd-based metal-organic framework electrochemical sensor for rapid detection of Rhodamine B, J. Solid State Chem. 303 (2021) 122508.
[5] Y. Zhong, R. Zha, W. Li, C. Lu, Y. Zong, D. Sun, C. Li, Y. Wang, Signal-on near-infrared photoelectrochemical aptasensors for sensing VEGF165 based on ionic liquid-functionalized Nd-MOF nanorods and in-site formation of gold nanoparticles, Anal. Chem. 94 (2022) 17835–17842.
[6] L. Fritea, F. Banica, T.O. Costea, L. Moldovan, L. Dobjanschi, M. Muresan, S. Cavalu, Metal nanoparticles and carbon-based nanomaterials for improved performances of electrochemical (Bio) sensors with biomedical applications, Materials 14 (2021) 6319.
[7] J. Zhu, X. Huang, W. Song, Physical and chemical sensors on the basis of laser-induced graphene: mechanisms, applications, and perspectives, ACS Nano 15 (2021) 18708–18741.
[8] I.J. Oh, D. Kim, S.-Y. Kim, S. Choi, W.-H. Yeo, H.-R. Lim, Advances in laser-induced graphene: materials, fabrication, and emerging applications in flexible electronics, Front. Nanotechnol. 7 (2025) 1750193.
[9] Y. Long, Y. Sun, L. He, R. Song, J. Zheng, X. Yang, Z. Peng, Z. Ma, W. Wang, J. Chen, Laser-processed micro/nano electrodes for integrated devices: architectures, mechanisms and prospects, Nano Res. 19 (2026) 94908668.
[10] T.D. Le, H. Phan, S. Kwon, S. Park, Y. Jung, J. Min, B.J. Chun, H. Yoon, S.H. Ko, S. Kim, Recent advances in laser-induced graphene: mechanism, fabrication,

properties, and applications in flexible electronics, Adv. Funct. Mater. 32 (2022) 2205158.
[11] Z. Ma, B.L. Khoo, Recent advances in laser-induced-graphene-based soft skin electronics for intelligent healthcare, Soft Sci. 4 (2024) 26.
[12] L. Du, W. Chen, J. Wang, W. Cai, S. Kong, C. Wu, Folic acid-functionalized zirconium metal-organic frameworks based electrochemical impedance biosensor for the cancer cell detection, Sens. Actuators, B Chem. 301 (2019) 127073.
[13] R. Geetha Bai, K. Muthoosamy, R. Tuvikene, H. Nay Ming, S. Manickam, Highly sensitive electrochemical biosensor using folic acid-modified reduced graphene oxide for the detection of cancer biomarker, Nanomaterials 11 (2021) 1272.
[14] A. Hashemzadeh, F. Amerizadeh, F. Asgharzadeh, M. Darroudi, A. Avan, S. M. Hassanian, M. Landarani, M. Khazaei, Delivery of oxaliplatin to colorectal cancer cells by folate-targeted UiO-66-NH2, Toxicol. Appl. Pharmacol. 423 (2021) 115573.
[15] W. Li, G. Tan, H. Zhang, Z. Wang, Y. Jin, Folate chitosan conjugated doxorubicin and pyropheophorbide acid nanoparticles (FCDP–NPs) for enhance photodynamic therapy, RSC Adv. 7 (2017) 44426–44437.
[16] S. Sanli, E. Tabak, N. Kilinc, A. Kösemen, M. Erginer, S. Öztürk, F.B. Barlas, Surface-Engineered TiO2 Film for Enhanced Electrochemical Biosensing and Cell Monitoring, 6, Analysis & Sensing, 2026 e202500072.
[17] Z.A. Suliman, A.A. Ibrahim, C.A. Mecha, M.N. Chollom, Photocatalytic degradation and antibacterial efficacy of novel synthesized green Cu–Fe metal organic framework derived from Acacia nilotica extract, Discover Chemistry 2 (2025) 219.
[18] F. Preischel, A. Ghazy, M. Seren, J. Obenlüneschloß, R. Mullins, D. Rogalla, T. Gemming, M. Nolan, J. Debus, M. Karppinen, Atomic and molecular layer deposition of Nd-and Eu-Based oxide and hybrid thin films: computationally guided precursor selection, Chem. Mater. 38 (9) (2026) 4422–4436.
[19] V. Ţucureanu, A. Matei, A.M. Avram, FTIR spectroscopy for carbon family study, Crit. Rev. Anal. Chem. 46 (2016) 502–520.
[20] Y. Ji, X. Yang, Z. Ji, L. Zhu, N. Ma, D. Chen, X. Jia, J. Tang, Y. Cao, DFT-calculated IR spectrum amide I, II, and III band contributions of N-methylacetamide fine components, ACS Omega 5 (2020) 8572–8578.
[21] B. Karaca, D. Sakarya, P. Siyah, A.M. Senisik, Y. Kaptan, F.C. Çavusoglu, D. S. Mansuroglu, S. Öztürk, S.S. Bayazit, F.B. Barlas, Dual-Functioning metal-organic frameworks: methotrexate-loaded gadolinium MOFs as drug carriers and radiosensitizers, Chem.–Eur. J. 31 (2025) e202404106.
[22] J. Luo, B.S. Liu, C. Cao, F. Wei, Neodymium (III) organic frameworks (Nd-MOF) as near infrared fluorescent probe for highly selectively sensing of Cu2+, Inorg. Chem. Commun. 76 (2017) 18–21.
[23] Y. Kumar, A.S.K. Sinha, K.D.P. Nigam, D. Dwivedi, J.S. Sangwai, Functionalized nanoparticles: tailoring properties through surface energetics and coordination chemistry for advanced biomedical applications, Nanoscale 15 (2023) 6075–6104.
[24] W. Zhu, G. Xiang, J. Shang, J. Guo, B. Motevalli, P. Durfee, J.O. Agola, E.N. Coker, C.J. Brinker, Versatile surface functionalization of metal–organic frameworks through direct metal coordination with a phenolic lipid enables diverse applications, Adv. Funct. Mater. 28 (2018) 1705274.
[25] R. Ye, D.K. James, J.M. Tour, Laser-induced graphene, Acc. Chem. Res. 51 (2018) 1609–1620.
[26] I.E. Valenzuela, J.C. Munoz-Acevedo, E. Pabón, A.P.S. Paim, Cu (II)-based metal-organic framework functionalized with graphene oxide as a sorbent for the dispersive micro-solid-phase extraction of losartan potassium from water, J. Porous Mater. 31 (2024) 1737–1752.
[27] S. Singh, K. Mitra, S. Senapati, R. Singh, Y. Biswas, S.K. Sen Gupta, N. Misra, T. K. Mandal, P. Maiti, B. Ray, Water soluble fluorescent graphene nanodots, ChemNanoMat 4 (2018) 1177–1188.
[28] H. Qu, L. Huang, Z. Han, Y. Wang, Z. Zhang, Y. Wang, Q. Chang, N. Wei, M. J. Kipper, J. Tang, A review of graphene-oxide/metal–organic framework composites materials: characteristics, preparation and applications, J. Porous Mater. 28 (2021) 1837–1865.
[29] A.M. Ross, Z. Jiang, M. Bastmeyer, J. Lahann, Physical aspects of cell culture substrates: topography, roughness, and elasticity, Small 8 (2012) 336–355.
[30] D. Bitounis, H. Ali-Boucetta, B.H. Hong, D. Min, K. Kostarelos, Prospects and challenges of graphene in biomedical applications, Adv. Mater. 25 (2013) 2258–2268.
[31] W.C. Lee, C.H.Y.X. Lim, H. Shi, L.A.L. Tang, Y. Wang, C.T. Lim, K.P. Loh, Origin of enhanced stem cell growth and differentiation on graphene and graphene oxide, ACS Nano 5 (2011) 7334–7341.
[32] P. Horcajada, R. Gref, T. Baati, P.K. Allan, G. Maurin, P. Couvreur, G. Férey, R. E. Morris, C. Serre, Metal–organic frameworks in biomedicine, Chem Rev 112 (2012) 1232–1268.
[33] J. Yang, Y. Yang, Metal–organic frameworks for biomedical applications, Small 16 (2020) 1906846.
[34] Y. Lu, P.S. Low, Folate-mediated delivery of macromolecular anticancer therapeutic agents, Adv. Drug Deliv. Rev. 54 (2002) 675–693.
[35] F.B. Barlas, D.A. Seleci, M. Ozkan, B. Demir, M. Seleci, M. Aydin, M.A. Tasdelen, H. M. Zareie, S. Timur, S. Ozcelik, Folic acid modified clay/polymer nanocomposites for selective cell adhesion, J. Mater. Chem. B 2 (2014) 6412–6421.
[36] K. Anselme, L. Ploux, A. Ponche, Cell/material interfaces: influence of surface chemistry and surface topography on cell adhesion, J. Adhes. Sci. Technol. 24 (2010) 831–852.
[37] D. Feng, Y. Song, W. Shi, X. Li, H. Ma, Distinguishing folate-receptor-positive cells from folate-receptor-negative cells using a fluorescence off–on nanoprobe, Anal. Chem. 85 (2013) 6530–6535.
[38] J.-M. Xia, X. Wei, X.-W. Chen, Y. Shu, J.-H. Wang, Folic acid modified copper nanoclusters for fluorescent imaging of cancer cells with over-expressed folate receptor, Microchim. Acta 185 (2018) 205.
[39] E. Seliverstova, N. Ibrayev, E. Alikhaidarova, E. Menshova, Optical properties of reduced graphene oxide nanodots prepared by laser ablation, Carbon Lett. 32 (2022) 1567–1576.
[40] M. Madni, Z. Ullah, H. Jiang, J. Roy, Y. Yan, D. Chen, Z. Jin, X. Wu, Y. Lan, S. Wang, Unraveling the hidden balance between quantum confinement and structural modifications in near-infrared fluorescent carbon dots, Chemical & Biomedical Imaging 4 (7) (2026) 1214–1247.
[41] S. Chung, R.A. Revia, M. Zhang, Graphene quantum dots and their applications in bioimaging, biosensing, and therapy, Adv. Mater. 33 (2021) 1904362.
[42] Y. Tepeli, B. Demir, S. Timur, U. Anik, An electrochemical cytosensor based on a PAMAM modified glassy carbon paste electrode, RSC Adv. 5 (2015) 53973–53978.
[43] J.J. Castillo, W.E. Svendsen, N. Rozlosnik, P. Escobar, F. Martínez, J. Castillo-León, Detection of cancer cells using a peptide nanotube–folic acid modified graphene electrode, Analyst 138 (2013) 1026–1031.
[44] S. Iqbal, S. Siddique, S. Kainat, H. Hafeez, A. Hafeez, F. Jabeen, S. Majeed, N. Sabir, M. Ahmed, M. Najam-ul-Haq, Synthesis and evaluation of folic acid functionalized magnetic nanoparticles as dual system for fluorescent imaging and electrochemical detection of circulating tumor cells, Microchem. J. (2026) 118068.
[45] J. Ni, Q. Wang, W. Yang, M. Zhao, Y. Zhang, L. Guo, B. Qiu, Z. Lin, H.-H. Yang, Immobilization free electrochemical biosensor for folate receptor in cancer cells based on terminal protection, Biosens. Bioelectron. 86 (2016) 496–501.
[46] C. Hu, G. Wei, F. Zhu, A. Wu, L. Luo, S. Shen, J. Zhang, Platinum-based nanocomposite Pt@ BSA as an efficient electrochemical biosensing interface for rapid and ultrasensitive determination of folate receptor-positive tumor cells, ACS Appl. Bio Mater. 5 (2022) 3038–3048.
[47] K.R. Kim, W. Yeo, Advances in sensor developments for cell culture monitoring, BMEMat 1 (2023) e12047.
[48] S. Arman, R.D. Tilley, J.J. Gooding, A review of electrochemical impedance as a tool for examining cell biology and subcellular mechanisms: merits, limits, and future prospects, Analyst 149 (2024) 269–289.
[49] L. Du, W. Chen, J. Wang, W. Cai, S. Kong, C. Wu, Folic acid-functionalized zirconium metal-organic frameworks based electrochemical impedance biosensor for the cancer cell detection, Sens. Actuators, B Chem. 301 (2019) 127073, https://doi.org/10.1016/J.SNB.2019.127073.
[50] R. Zha, H. Liang, Y. Zong, L. Chen, X. Chen, H. Deng, X. Xiong, H. Zhang, X. Li, C. Li, Y. Wang, Responsive Nd-MOF nanorods based near-infrared photoelectrochemical cytosensor and real-time monitoring HClO releasing from cells and tumor, Sens. Actuators, B Chem. 405 (2024) 135291, https://doi.org/10.1016/J.SNB.2024.135291.
[51] F. Duan, M. Hu, C. Guo, Y. Song, M. Wang, L. He, Z. Zhang, R. Pettinari, L. Zhou, Chromium-based metal-organic framework embedded with cobalt phthalocyanine for the sensitively impedimetric cytosensing of colorectal cancer (CT26) cells and cell imaging, Chem. Eng. J. 398 (2020) 125452, https://doi.org/10.1016/J.CEJ.2020.125452.
[52] D. Ou, D. Sun, Z. Liang, B. Chen, X. Lin, Z. Chen, A novel cytosensor for capture, detection and release of breast cancer cells based on metal organic framework PCN-224 and DNA tetrahedron linked dual-aptamer, Sens. Actuators, B Chem. 285 (2019) 398–404, https://doi.org/10.1016/J.SNB.2019.01.079.
[53] A.A. Zare, H. Naderi-Manesh, S.M. Naghib, M. Shamsipur, F. Molaabasi, Label-free electrochemical cancer cell detection leveraging hemoglobin-encapsulated silver nanoclusters and Cu-MOF nanohybrids on a graphene-assisted dual-modal probe, Sci. Rep. 13 (1) (2023) 21980, https://doi.org/10.1038/s41598-023-49418-1, 2023 13.
[54] T.T. Zheng, R. Zhang, L. Zou, J.J. Zhu, A label-free cytosensor for the enhanced electrochemical detection of cancer cells using polydopamine-coated carbon nanotubes, Analyst 137 (2012) 1316–1318, https://doi.org/10.1039/C2AN16023D.